

Article

In Situ Observation for Deformation-Induced Martensite Transformation (DIMIT) during Tensile Deformation of 304 Stainless Steel Using Neutron Diffraction. PART I: Mechanical Response

Yusuke Onuki ^{1,*}  and Shigeo Sato ² 

¹ Frontier Research Center for Applied Atomic Sciences, Ibaraki University 162-1 Shirakata, Tokai, Ibaraki 319-1106, Japan

² Graduate School of Science and Engineering, Ibaraki University 4-12-1 Nakanarusawa, Hitachi, Ibaraki 316-8511, Japan; shigeo.sato.ar@vc.ibaraki.ac.jp

* Correspondence: yusuke.onuki.0@vc.ibaraki.ac.jp; Tel.: +81-29-352-3234

Received: 14 July 2020; Accepted: 10 September 2020; Published: 11 September 2020



Abstract: 304 stainless steel is one of the most common stainless steels due to its excellent corrosion resistance and mechanical properties. Typically, a good balance between ductility and strength derives from deformation-induced martensite transformation (DIMIT), but this mechanism has not been fully explained. In this study, we conducted in situ neutron diffraction measurements during the tensile deformation of commercial 304 stainless steel (at room temperature) by means of a Time-Of-Flight type neutron diffractometer, iMATERIA (BL20), at J-PARC MLF (Japan Proton Accelerator Research Complex, Materials and Life Science Experimental Facility), Japan. The fractions of α' -(BCC) and ϵ -(HCP) martensite were quantitatively determined by Rietveld-texture analysis, as well as the anisotropic microstrains. The strain hardening behavior corresponded well to the microstrain development in the austenite phase. Hence, the authors concluded that the existence of martensite was not a direct cause of hardening, because the dominant austenite phase strengthened to equivalent values as in the martensite phase. Moreover, the transformation-induced plasticity (TRIP) mechanism in austenitic steels is different from that of low-alloy bainitic TRIP steels.

Keywords: TRIP effect; neutron diffraction; 304 stainless steel

1. Introduction

Austenitic stainless steels are widely used in industries because they have both superior corrosion resistance and mechanical properties. The most commonly used grade is JIS-SUS304 (equivalent to AISI 304), which contains mainly 18 mass% Cr, 8 mass% Ni, and less than 0.08 mass% C. In this steel, the FCC austenite (γ phase) is a metastable phase at room temperature. The more stable BCC martensite (α' phase) is obtained by deformation-induced martensite transformation (DIMIT) when the steel is plastically deformed. It is well known that DIMIT leads to a high-strain hardening rate, resulting in a very large elongation until the tensile stress is achieved [1,2]. To address the role of DIMIT in detail, many studies have been conducted using DIMIT in 304 stainless steel, but the involved mechanism has not been fully addressed to date. This may be due to the reasons explained as follows:

HCP ϵ martensite may (or may not) be formed in Cr-Ni steels by DIMIT. The existence of ϵ martensite in 18Cr-8Ni steel was first confirmed in the 1950s. However, Nishiyama showed that the occurrence of ϵ martensite is strongly affected by chemical composition, microstructure, and temperature [3]. Such factors also affect the route of DIMIT, i.e., whether it will proceed as $\gamma \rightarrow \epsilon \rightarrow \alpha'$ or the simultaneous $\gamma \rightarrow \alpha'$ and $\gamma \rightarrow \epsilon$ transformations occur [4,5].

In addition, the quantitative detection of HCP martensite is difficult compared to the detection of α' (BCC) martensite. The amount of α' martensite can be determined accurately by saturated magnetization measurements [5]. In the case of nonmagnetic ϵ martensite, microscopy and diffraction measurements are used, but the results frequently have large uncertainties because of statistic reliability and sharp textures analysis, respectively.

Grosse et al. and Kalkhof et al. attempted to use the fraction of α' martensite as an indicator of accumulated plastic strain by low-cycle fatigue for AISI 321 (18Cr-10Ni) steel [6,7]. They found a linear relationship between the martensite fraction and the number of cycles. However, the slope of the linear fitting regression strongly depended on the initial state. The existence of ϵ martensite was not mentioned in those studies. However, Tiamiyu et al. confirmed ϵ martensite by XRD and EBSD after the compressive deformation of AISI 321 [8], although it disappeared with increasing strain. They also pointed out that the developments of α' and ϵ martensite are dependent on the initial grain size.

The authors recently reported that the neutron-diffraction-based Rietveld texture analysis (NDRTA) can be a powerful tool for the quantitative detection of both ϵ and α' martensite in 18Cr-8Ni steels [5]. In this study, the authors applied this technique for in situ observation during the tensile deformation of a 304 stainless steel sheet sample.

This study consists of two successive papers. In part I, we report the relationship between the fraction of martensite phases and the corresponding mechanical behavior. In addition, the line profile analysis, as part of the NDRTA, was assessed to discuss the role of dislocation hardening. In part II, the mechanism of DIMT will be discussed from the texture point of view.

2. Materials and Methods

2.1. Materials

A commercial SUS304 stainless steel sheet with a thickness of 2 mm was evaluated. The chemical composition is presented in Table 1. Figure 1a shows the initial grain structure of SUS304 that was observed by electron backscattered diffraction (EBSD), using a Hitachi SU-5000 electron microscope equipped with EDAX OIM system. It was observed that the sample had a fully recrystallized grain structure with annealing twins. The average grain size was 19 μm . No secondary phase was confirmed by EBSD, nor by neutron diffraction. A weak rolling texture was confirmed, but the maximum pole density on any pole figure was less than 2.

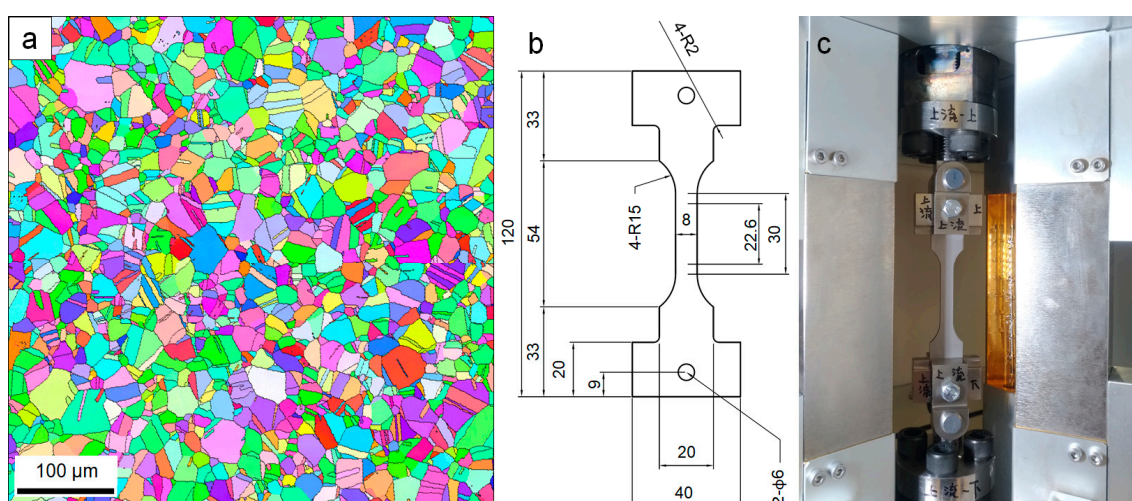


Figure 1. (a) Initial grain structure of the sample, (b) shape of the tensile coupon, and (c) image of the coupon fixed on the deformation-testing machine.

A tensile coupon (Figure 1b) was prepared by spark cutting of the SUS304 sheet. The basic design of the coupon was Type 14B, as defined in JIS Z 2201. However, to fix the coupon with minimum

volume of the anvils, additional wings, 40 mm in width, were added to both ends. Loading was achieved by hooking these wings to the protrusions of anvils, as shown in Figure 1c. The deformation tests were conducted at room temperature (300 K).

Table 1. Chemical composition of the tested steel (mass%).

Element	C	Si	Mn	P	S	Ni	Cr	Cu	N	Fe
	0.042	0.52	0.92	0.030	0.002	8.08	18.26	0.22	0.052	Balance

2.2. In Situ Neutron Diffraction Experiments

The Time-Of-Flight (TOF) neutron diffractometer, iMATERIA, at Japan Proton Accelerator Research Complex in Materials and Life Science Experimental Facility (J-PARC MLF, Tokai, Japan) was used in this study [9]. As shown in Figure 2, iMATERIA has numerous detectors surrounding the incident neutron beam. The detectors were divided into small areas called observation points (OPs) and categorized into 7 bank groups. Each bank group consisted of OPs having almost the same 2θ angles. For example, 2θ angles for the OPs of Bank 31 were approximately 31° .

The deformation-testing machine was installed in the sample chamber of iMATERIA, which enabled uniaxial deformation along Y_D . The testing machine was set inclined so that the components of the machine did not obstruct the diffraction beam paths to the OPs. However, the tensile coupon was set so that the ND was parallel to X_D , the incident beam direction.

The deformation test was conducted with a constant crosshead speed of 0.03 mm/min without stopping the deformation. The neutron scattering data at every OP was constantly acquired during the test. The acquired neutron diffraction data was divided into an 1800 s acquisition time increment, which corresponded to a true strain increment of approximately 0.02–0.025. Note that the test was interrupted before breaking point due to limitations of the testing machine at that time.

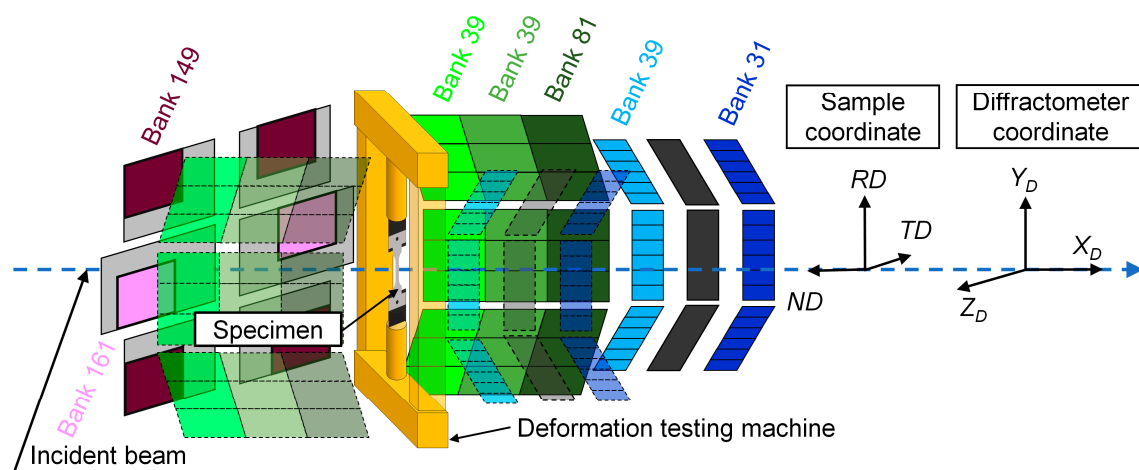


Figure 2. Schematic of iMATERIA equipped with the deformation-testing machine.

2.3. Analysis

The neutron diffraction data was analyzed using MAUD software (version 2.9.3), based on the method called Rietveld texture analysis (RTA) [9–13]. The analysis comprises the simultaneous and interactive refinement of textures and diffraction patterns fitting, which can quantitatively determine the phase fractions of γ austenite and α' or ϵ martensite. The result of the texture analysis is reported in a separate paper.

Herein, the macroscopic stress correction was conducted. The “moment pole stress” model was applied for the γ austenite and α' martensite phases, to fit the peak shifts due to the external stress. This model calculates the bulk elastic modulus from the single crystalline stiffness, considering the

texture of the sample. In this study, we used the weighted Hill's model to connect the bulk and single crystalline elastic modulus. As it is well known, the original Hill's (or Voigt–Reuss–Hill) model calculates the bulk elastic compliance as an arithmetic mean of the Voigt and Reuss values. On the one hand, the weighted Hill's model calculates the weighted average of them [14]. The weight is called “Voigt–Reuss ratio” in MAUD, which can be refined as one of the parameters in RTA.

The elastic stiffness values used in this study were: $C_{11} = 209$ GPa, $C_{12} = 133$ GPa, and $C_{44} = 121$ GPa for the γ phase [15], and $C_{11} = 230$ GPa, $C_{12} = 135$ GPa, and $C_{44} = 117$ GPa for the α' phase [16]. For the ε phase, it was not possible to apply the same method since the corresponding elastic stiffness values were not available. The “real” lattice parameters for this phase were also difficult to determine, because the ε phase appeared during loading with relatively strong texture. Hence, the isotropic elastic model was applied for the ε phase.

To evaluate the line broadening of the diffraction peak, we applied the “Popa rules” [17] model to the MAUD software [12]. This is actually equivalent to the line broadening treatment on the modified Williamson–Hall method suggested by Ungár et al. [18]. For a better understanding of this model, we will describe its basic theory.

The simplest model for the line profile analysis was proposed by Williamson and Hall [19], which is

$$\Delta K = \langle \varepsilon \rangle K + A/D \quad (1)$$

where $K = 2\sin\theta/\lambda$, ΔK is the peak breadth, D is the crystallite size, $\langle \varepsilon \rangle$ is the root-square-mean microstrain, and A is a constant that can vary depending on how the peak breadths are evaluated. However, due to the anisotropic features of the crystal and dislocation, a perfect linear relationship between K and ΔK was merely observed. Hence, an advanced treatment was suggested as the modified Williamson–Hall (mWH) method [18,20], expressed as follows:

$$\Delta K = O(K\sqrt{C})^2 + \varphi K\sqrt{C} + 1/D. \quad (2)$$

The notable feature in the above equation was the introduction of the contrast factor, C . The first squared term, $O(K\sqrt{C})^2$, is negligibly small. C is defined as follows:

$$C = C_{h00} \frac{1}{(h^2 + k^2 + l^2)^2} \left\{ (h^4 + k^4 + l^4) + (2 - q)(h^2k^2 + k^2l^2 + l^2h^2) \right\}, \quad (3)$$

where C_{h00} is a constant and q is the factor related to the ratio of screw and edge dislocations. In Equation (2), φ can be found as the slope when plotting ΔK against $K\sqrt{C}$.

On the other hand, Popa proposed a similar model to fit the anisotropic line broadening in the Rietveld analysis [17]. This model suggests the variation of $\langle \varepsilon \rangle$ in Equation (1) depending on hkl . For a cubic crystal, the following derives:

$$\langle \varepsilon_{hkl}^2 \rangle = \frac{1}{(h^2 + k^2 + l^2)^2} \left\{ e_0^2 (h^4 + k^4 + l^4) + 2 \frac{e_1}{|e_1|} e_1^2 (h^2k^2 + k^2l^2 + l^2h^2) \right\}, \quad \langle \varepsilon_{hkl} \rangle = \sqrt{\langle \varepsilon_{hkl}^2 \rangle}, \quad (4)$$

where coefficients e_0 and e_1 are refined parameters in the Rietveld analysis. Note that Equation (4) was slightly modified from Popa's original equation in order to be implemented in MAUD software. Since Equations (3) and (4) are essentially identical, it follows

$$\varphi^2 C_{h00} = e_0^2, \quad \varphi^2 C_{h00} (2 - q) = \frac{e_1}{|e_1|} e_1^2. \quad (5)$$

Even if not calculated in this study, Equation (5) may enable to determine the quantitative ratio of screw and edge dislocations by RTA. Herein, the development of $\langle \varepsilon_{100} \rangle$, $\langle \varepsilon_{110} \rangle$, and $\langle \varepsilon_{111} \rangle$ was separately determined.

3. Results

From the true stress–true strain curve (Figure 3a), a stable, mostly, monotonic strain hardening was observed, as frequently reported in the literature [1]. The strain hardening rate (θ) was calculated as $\theta = d\sigma/dE$, as shown in Figure 3b. In this study, E represents the macroscopic true strain to distinguish it from the microstrain ($\langle\epsilon\rangle$), and the ϵ (HCP) martensite. We calculated $\theta = d\sigma/dE$ in the following two ways: (1) a simple calculation from stress and strain increments, $\Delta\sigma$ and ΔE , observed during a certain period (θ_1) and (2) analytical derivation of the fitting curve for $\sigma(E)$ using a 6th-order polynomial function (θ_2). The latter gives a smooth curve, which has its minimum at a true strain of 0.24.

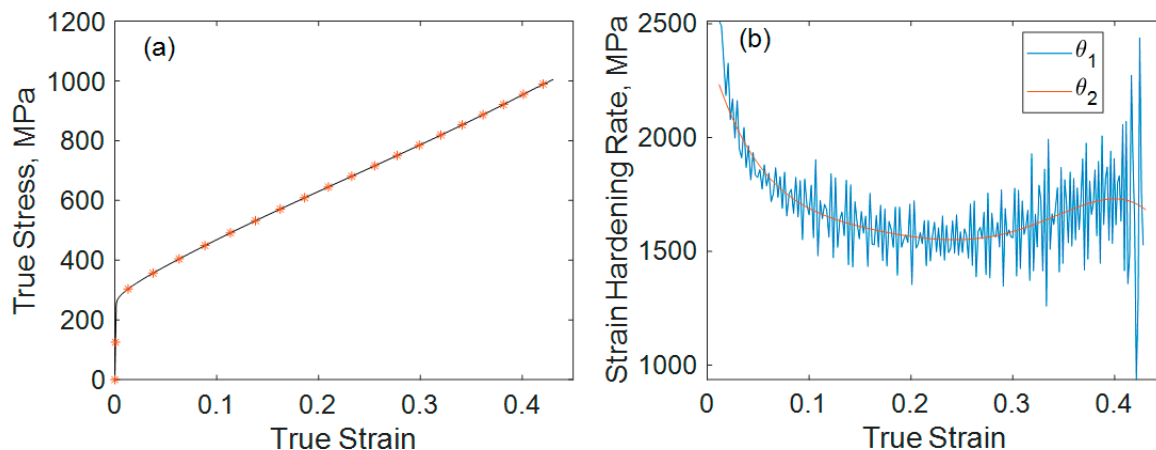


Figure 3. (a) True stress–true strain curve and centers for the analyzed intervals and (b) strain hardening rates shown as a function of true strain. θ_1 and θ_2 were defined as $\Delta\sigma/\Delta E$ in 100 s, and the differential curve for $\sigma(E)$ was fitted using a 6th-order polynomial function, respectively.

Figure 4 shows the diffraction patterns around the onset point of DIMT. First, 110ϵ peaks appeared at $E = 0.09$. However, the peak was too small to conduct quantitative fitting. At $E = 0.11$, the fitting for ϵ was possible, and we calculated a 1.4 vol% fraction, which was the lowest limit of detection in the current analysis. Hence, a small amount of ϵ -martensite might be formed at an earlier stage of deformation. In contrast, the onset of α' martensite formation at $E = 0.14$ was a little more evident; in this case, due to the high crystal symmetry of α' martensite, the lowest detection limit was 0.7 vol%.

Figure 5 illustrates the increase in the volume fractions of α' and ϵ martensite, $V\alpha$ and $V\epsilon$, with increasing strain. Note that the analyzed phase fractions might have larger errors than the analytically determined standard uncertainties, which were quite small. In both the qualitative (experimentally observed) and the quantitative (computer-based) analyses, the minor phase detection corresponds to distinguishing the diffraction peak from background fluctuation. When a background pattern has a large fluctuation, small diffraction peaks are difficult to be found. Even if the diffraction peaks are high enough to be observed, the background uncertainty directly relates to the uncertainty of the estimated diffraction intensity; i.e., the phase fraction. Hence, the authors estimate the error or uncertainty of the phase fraction analysis to be almost equal to the lowest detection limit, which was around 1–2%.

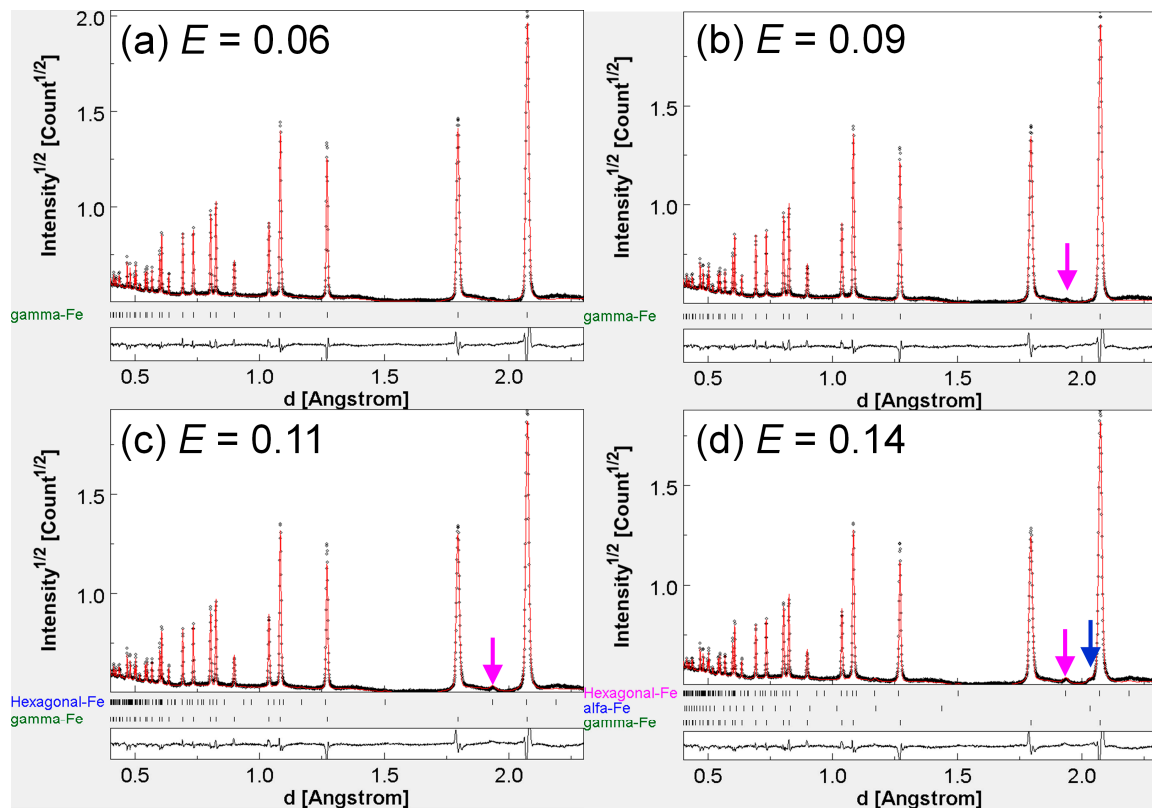


Figure 4. Average diffraction patterns observed in Bank 81 at different strains. The pink and blue arrows indicate 110ϵ and 110α diffraction peaks, respectively.

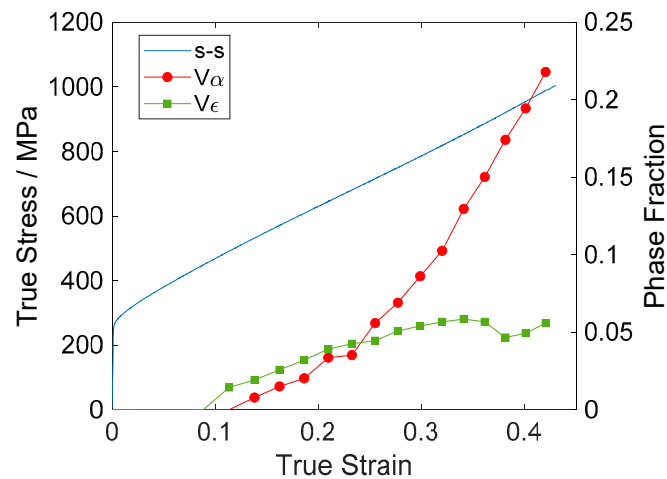


Figure 5. Change in volume fractions of α' (V_{α}) and ϵ (V_{ϵ}) martensite along with the true stress–true strain curve. The standard uncertainties were smaller than the markers (i.e., $<1 \times 10^{-3}$).

4. Discussion

4.1. Analysis of Stress–Strain Curve

Miura et al. suggested a method to determine the strain E_{MS} at which DIMT may start, when fitting the true stress–true strain curve [21]. Considering that their deformation test was conducted at 77 K, the sigmoidal, two-step hardening behavior was evident. Hence, they fitted the low strain (without DIMT) and high strain (with DIMT) regions using the well-known relationship, $\sigma = KE^n$. The coefficient n for each of the two regions was n_1 and n_2 , respectively. This approach was adopted to

analyze our results, as shown in Figure 6. Since the current deformation test was conducted at room temperature, the transition from $\sigma = K_1 E^{n_1}$ to $\sigma = K_2 E^{n_2}$ was unclear. However, the cross point of the two fitting curves was $E_{MS} = 0.11$. This is in good agreement with the strain value where the ϵ and α' martensite first appear on the neutron diffraction pattern (Figure 5). Hence, the approach seemed to be valid to describe the stress–strain behavior with DIMT. However, this does not correspond to the point of the acceleration of the strain hardening, $E = 0.24$, shown in Figure 3b. This is rather related to the strain where the n_2 curve starts fitting exactly the experimental stress–strain curve.

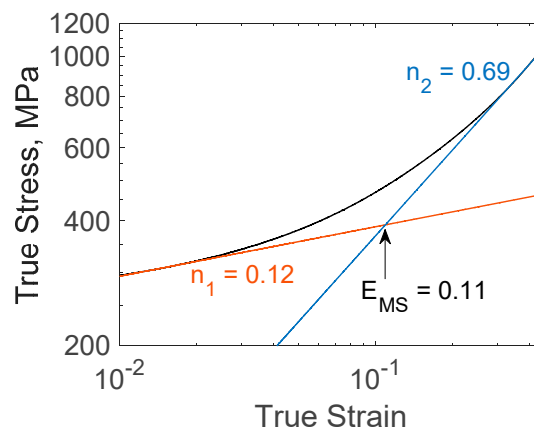


Figure 6. True stress–true strain curve in double-log plot (black curve). Fitting curves using $\sigma = K_1 E^{n_1}$ and $\sigma = K_2 E^{n_2}$ are shown as the orange and blue curves, respectively. The fitted regions were $0.012 \leq E \leq 0.018$ and $0.030 \leq E \leq 0.430$, for the n_1 and n_2 curves, respectively.

4.2. Dislocation Hardening

Since the fitting using $\sigma = KE^n$ was a phenomenological approach, the microscopic hardening mechanism should be discussed from a different approach. In this section, the degree of dislocation hardening is considered. Dislocation hardening is often modeled using the Bailey–Hirsch equation, $\Delta\sigma_{disl} = M\alpha\mu b\sqrt{\rho}$, where α is a constant, M is the Taylor factor, μ is the shear modulus, b is the length of Burgers vector, and ρ is the dislocation density. As previously stated, $\langle\epsilon\rangle$ (or φ in the mWH description) is proportional to $\sqrt{\rho}$, so $\Delta\sigma_{disl} \propto \langle\epsilon\rangle$. In Figure 7, the development curves of $\langle\epsilon_{100}\rangle$, $\langle\epsilon_{110}\rangle$, and $\langle\epsilon_{111}\rangle$ for austenite as a function of true strain are shown. It is known that austenitic stainless steel has a large elastic anisotropy [15]. Hence, it is accepted that the softest direction $\langle 100 \rangle$ exhibits a large scatter of lattice plane displacement (i.e., microstrain); $\langle 111 \rangle$ is the hardest and $\langle 110 \rangle$ is an intermediate direction.

As indicated by Equation (3) and Equation (5), $\langle\epsilon_{100}\rangle$ is a function of $e_0 = \varphi\sqrt{C_{h00}}$ that is not affected by e_1 . Hence, we can observe that $\langle\epsilon_{100}\rangle \propto \varphi \propto \sqrt{\rho}$. The good correspondence between $\langle\epsilon_{100}\rangle$ and the true stress–true strain curve in Figure 7 indicates that the hardening behavior can be described by dislocation hardening in austenite.

Therefore, the strengthening by DIMT was not due to the existence of plastically hard martensite particles, but due to the enhancement of dislocation hardening. In other words, austenite was as strong as deformation-induced martensite, at any stage of deformation. In contrast, for the so-called low-alloy TRIP steels, martensite formed by DIMT is much stronger than the preexisting phases, and in fact, the one causing strain hardening [22]. The mechanisms of the TRIP effects in the two kinds of steels should be considered separately.

At the true strain of approximately 0.24, the increases of $\langle\epsilon_{110}\rangle$ and $\langle\epsilon_{111}\rangle$ were accelerated. A true strain of 0.24 was the point where the strain-hardening rate started to increase, as shown in Figure 3b. In addition, this was approximately the start point where the n_2 curve in Figure 6 fitted the s–s curve as well. The increase for α' martensite was also accelerated around $E = 0.24$.

The acceleration effect was observed for $\langle \epsilon_{110} \rangle$ and $\langle \epsilon_{111} \rangle$, but not for $\langle \epsilon_{100} \rangle$. This was due to the increase of the coefficient e_1 in Equation (4). According to Equation (5), this corresponds to the decrease in q ; i.e., an increase in the ratio of edge dislocations to the screw ones. Although further microstructural studies are needed, this may explain why the dislocation hardening was not exhausted even at large strains. Since the edge dislocation cannot experience cross slipping, this has less opportunity for recovery compared to that of screw dislocations.

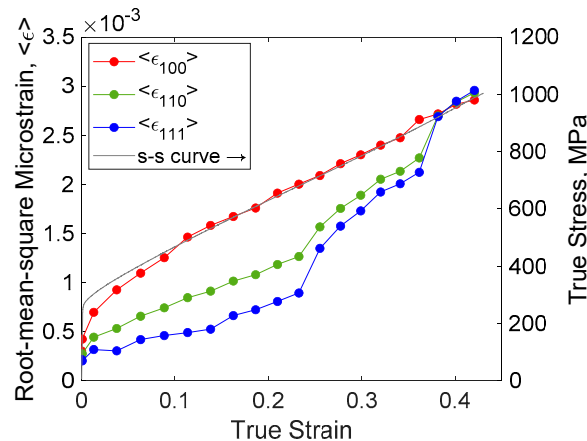


Figure 7. Development of microstrain $\langle \epsilon_{hkl} \rangle$ along $\langle 100 \rangle$, $\langle 110 \rangle$, and $\langle 111 \rangle$ as a function of true strain. The ranges and scales for the left and right vertical axes were arbitrarily determined to show the qualitative correspondence. The standard uncertainties for microstrain were smaller than the markers (i.e., $< 2 \times 10^{-5}$).

4.3. Chemical Stability of Austenite

The stability of austenite against DIMT is frequently expressed by the factor Md_{30} . The most used equation to calculate Md_{30} was suggested by Nohara et al. [23]. Using the composition presented in Table 1, Md_{30} resulted to be 277 K. Masumura et al. recently revised this equation and suggested an alternative equation, when separating the roles of C and N [24]. According to their equation, the calculated Md_{30} was 303 K. Since their equation did not include the effect of Cu, we considered it by applying the coefficient suggested by Nohara et al. Then we obtained 297 K. As seen in Figure 5, at a true strain of 0.31, volume fractions of α' and ϵ martensite were 6.9% and 5.1%, respectively. Therefore, Md_{30} , the temperature where 50% volume fraction of α' is achieved at a true strain of 0.3, should be much lower than the test temperature, 300 K. Hence, the evaluated case happened to be away from the Masumura's equation. As pointed out by them, the validity of the combining effects of all the variables into a simple equation must be carefully revised.

The study addressed the 18Cr-8Ni steels containing only C or N. The effect of adding N was coupled with the effect of adding C. However, they also reported that N- and C-added 18Cr-8Ni steels led to different morphologies of martensite [4,24]. According to these studies, C-added steels showed a $\gamma \rightarrow \epsilon \rightarrow \alpha'$ DIMT route, but the N-added steel exhibited $\gamma \rightarrow \alpha'$. Hence, when the steel contains both C and N, the analysis would be more complex. Additionally, Masumura et al. omitted the effect of the average grain size on Md_{30} . Tamiyu et al. reported that the grain size seems to be a factor to determine if $\gamma \rightarrow \epsilon \rightarrow \alpha'$ DIMT occurs and the fraction of α' martensite that may be obtained at a certain strain [8].

Although Nohara's equation resulted in a more feasible value, $Md_{30} = 277$ K, there is no scientific reason to conclude this is more valid. Since the current sample has a similar composition to that used by Nohara et al., their phenomenological equation led to a suitable prediction. To obtain a better prediction for DIMT in austenitic steels, further studies will be necessary on the conditions and the mechanism of the $\gamma \rightarrow \epsilon \rightarrow \alpha'$ type DIMT.

5. Conclusions

In situ Time-Of-Flight type neutron diffraction during the tensile test of 304 stainless steel (18Cr-8Ni) was conducted to observe the deformation-induced martensite transformation (DIMIT). As the strain increased, the ε (HCP) martensite first appeared followed by α' martensite formation at the true strain of 0.11. This strain corresponded to the transition of the strain hardening state without DIMIT to the state with DIMIT. However, the transient region corresponded to a true strain approximately in the range of 0.02–0.2. A clear acceleration of strain hardening was confirmed, at a true strain of 0.24; this also led to accelerate the increase in α' martensite fraction. Together, the increase of microstrain along $\langle 111 \rangle$ and $\langle 110 \rangle$ accelerated. The mechanical behavior of this metastable austenitic steel was mainly governed by dislocation structure in the austenite phase. The deformation-induced martensite may play a specific role in the development of dislocation structure in austenite, rather than supporting large stress as the hard particles in the tested steels.

Author Contributions: Conceptualization and methodology, Y.O. and S.S.; validation, formal analysis, investigation, and writing—original draft preparation, Y.O.; writing—review and editing and supervision, S.S. All authors have read and agreed to the published version of the manuscript.

Funding: This research was funded by Ibaraki prefecture local government.

Acknowledgments: The authors appreciate for the kind support by iMATERIA team, Ibaraki University, and staff of J-PARC MLF. The neutron experiment was conducted as a part of the research proposal 2019PM3002. The authors also acknowledge YONEKURA MFG Co., Ltd. for developing the special deformation-testing machine for the in situ neutron diffraction experiment.

Conflicts of Interest: The authors declare no conflict of interest.

References

1. Tsuchida, N.; Morimoto, Y.; Tonan, T.; Shibata, Y.; Fukaura, K.; Ueji, R. Stress-Induced Martensitic Transformation Behaviors at Various Temperatures and Their TRIP Effects in SUS304 Metastable Austenitic Stainless Steel. *ISIJ Int.* **2011**, *51*, 124–129. [\[CrossRef\]](#)
2. Angel, T. Formation of Martensite in Austenitic Stainless Steels. *J. Iron Steel Inst.* **1954**, *177*, 165–174.
3. Nishiyama, Z. *Martensitic Transformation*; Fine, M.E., Meshii, M., Wayman, C.M., Eds.; Academic Press Inc.: New York, NY, USA, 1978.
4. Masumura, T.; Nakada, N.; Tsuchiyama, T.; Takaki, S.; Koyano, T.; Adachi, K. The difference in thermal and mechanical stabilities of austenite between carbon- and nitrogen-added metastable austenitic stainless steels. *Acta Mater.* **2015**, *84*, 330–338. [\[CrossRef\]](#)
5. Onuki, Y.; Masumura, T.; Tsuchiyama, T.; Sato, S.; Tomida, T.; Takaki, S. Mutual Verification of Phase Fraction Analysis Techniques for Steels Comprising Deformation Induced Martensite Phases: Neutron-Diffraction-Based Rietveld Texture Analysis and Saturation Magnetization Measurement. *Tetsu-to-Hagane* **2020**, *106*, 457–464. [\[CrossRef\]](#)
6. Grosse, M.; Kalkhof, D.; Niffenegger, M.; Keller, L. Influencing parameters on martensite transformation during low cycle fatigue for steel AISI 321. *Mater. Sci. Eng. A* **2006**, *437*, 109–113. [\[CrossRef\]](#)
7. Kalkhof, D.; Grosse, M.; Niffenegger, M.; Leber, H.J. Monitoring fatigue degradation in austenitic stainless steels. *Fatigue Fract. Eng. Mater. Struct.* **2004**, *27*, 595–607. [\[CrossRef\]](#)
8. Tamiyu, A.; Tari, V.; Szpunar, J.; Odeshi, A.G.; Khan, A. Effects of grain refinement on the quasi-static compressive behavior of AISI 321 austenitic stainless steel: EBSD, TEM, and XRD studies. *Int. J. Plast.* **2018**, *107*, 79–99. [\[CrossRef\]](#)
9. Onuki, Y.; Hoshikawa, A.; Sato, S.; Ishigaki, T. Rapid Measurement of Texture of Metals by Time-of-Flight Neutron Diffraction at iMATERIA and its Applications. *Mater. Sci. Forum* **2016**, *879*, 1426–1430. [\[CrossRef\]](#)
10. Lutterotti, L.; Matthies, S.; Wenk, H.-R.; Schultz, A.S.; Richardson, J.W. Combined texture and structure analysis of deformed limestone from time-of-flight neutron diffraction spectra. *J. Appl. Phys.* **1997**, *81*, 594–600. [\[CrossRef\]](#)
11. Lutterotti, L.; Chateigner, D.; Ferrari, S.; Ricote, J. Texture, residual stress and structural analysis of thin films using a combined X-ray analysis. *Thin Solid Films* **2004**, *450*, 34–41. [\[CrossRef\]](#)

12. Wenk, H.-R.; Lutterotti, L.; Vogel, S.C. Rietveld texture analysis from TOF neutron diffraction data. *Powder Diffr.* **2010**, *25*, 283–296. [[CrossRef](#)]
13. Onuki, Y.; Hoshikawa, A.; Sato, S.; Ishigaki, T.; Tomida, T. Quantitative phase fraction analysis of steel combined with texture analysis using time-of-flight neutron diffraction. *J. Mater. Sci.* **2017**, *52*, 11643–11658. [[CrossRef](#)]
14. Murray, C.E. Equivalence of Kröner and weighted Voigt-Reuss models for X-ray stress determination. *J. Appl. Phys.* **2013**, *113*, 153509. [[CrossRef](#)]
15. Ledbetter, H.M. *Predicted Single-Crystal Elastic Constants of Stainless Steel 304*; Reed, R.P., Simon, N.J., Eds.; U.S. Department of Commerce, National Bureau of Standards: Washington, DC, USA, 1981; p. 648.
16. Kim, S.A.; Johnson, W.L. Elastic constants and internal friction of martensitic steel, ferritic-pearlitic steel, and α -iron. *Mater. Sci. Eng. A* **2007**, 633–639. [[CrossRef](#)]
17. Popa, N.C. The (hkl) Dependence of Diffraction-Line Broadening Caused by Strain and Size for all Laue Groups in Rietveld Refinement. *J. Appl. Crystallogr.* **1998**, *31*, 176–180. [[CrossRef](#)]
18. Ungár, T.; Borbély, A. The effect of dislocation contrast on X-ray line broadening: A new approach to line profile analysis. *Appl. Phys. Lett.* **1996**, *69*, 3173–3175. [[CrossRef](#)]
19. Williamson, G.; Hall, W. X-ray line broadening from filed aluminium and wolfram. *Acta Met.* **1953**, *1*, 22–31. [[CrossRef](#)]
20. Takaki, S.; Masumura, T.; Tsuchiyama, T. Dislocation Characterization by the Direct-fitting/modified Williamson–Hall (DF/mWH) Method in Cold Worked Ferritic Steel. *ISIJ Int.* **2019**, *59*, 567–572. [[CrossRef](#)]
21. Miura, R.; Ohnishi, K.; Nakajima, H.; Shimamoto, S. Effects of Carbon and Nitrogen on the Tensile Deformation Behavior of SUS304 and 316 Stainless Steels at Cryogenic Temperatures. *Tetsu-to-Hagane* **1987**, *73*, 715–722. [[CrossRef](#)]
22. Yamashita, T.; Morooka, S.; Harjo, S.; Kawasaki, T.; Koga, N.; Umezawa, O. Role of retained austenite in low alloy steel at low temperature monitored by neutron diffraction. *Scr. Mater.* **2020**, *177*, 6–10. [[CrossRef](#)]
23. Nohara, K.; Ono, Y.; Ohashi, N. Composition and Grain Size Dependencies of Strain-induced Martensitic Transformation in Metastable Austenitic Stainless Steels. *Tetsu-to-Hagane* **1977**, *63*, 772–782. [[CrossRef](#)]
24. Masumura, T.; Fujino, K.; Tsuchiyama, T.; Takaki, S.; Kimura, K. Effect of Carbon and Nitrogen on M30 in Metastable Austenitic Stainless Steel. *Tetsu-to-Hagane* **2019**, *105*, 1163–1172. [[CrossRef](#)]



© 2020 by the authors. Licensee MDPI, Basel, Switzerland. This article is an open access article distributed under the terms and conditions of the Creative Commons Attribution (CC BY) license (<http://creativecommons.org/licenses/by/4.0/>).